7-1-2004

Physical Conditions in Orion's Veil

N. P. Abel
University of Kentucky

C. L. Brogan
Institute for Astronomy

Gary J. Ferland
University of Kentucky, gary@uky.edu

C. R. O'Dell
Vanderbilt University

G. Shaw
University of Kentucky

See next page for additional authors

The Astrophysical Journal, 609:247–260, 2004 July 1

PHYSICAL CONDITIONS IN ORION'S VEIL

N. P. Abel,[1] C. L. Brogan,[2] G. J. Ferland,[1] C. R. O'Dell,[3] G. Shaw,[1] and T. H. Troland[1]

Received 2003 December 13; accepted 2004 March 15

ABSTRACT

Orion's veil consists of several layers of largely neutral gas lying between us and the main ionizing stars of the Orion Nebula. It is visible in 21 cm H I absorption and in optical and UV absorption lines of H I and other species. Toward θ^1 Ori C, the veil has two remarkable properties, a high magnetic field ($\approx$100 μG) and a surprising lack of H_2, given its total column density. Here we compute photoionization models of the veil to establish its gas density and its distance from θ^1 Ori C. We use a greatly improved model of the H_2 molecule that determines level populations in 10^5 rotational/vibrational levels and provides improved estimates of H_2 destruction via the Lyman-Werner bands. Our best-fit photoionization models place the veil 1–3 pc in front of the star at a density of 10^3–10^4 cm^{-3}. Magnetic energy dominates the energy of nonthermal motions in at least one of the 21 cm H I velocity components. Therefore, the veil is the first interstellar environment in which magnetic dominance appears to exist. We find that the low ratio of H_2/H^0 ($<10^{-4}$) is a consequence of high UV flux incident on the veil due to its proximity to the Trapezium stars and the absence of small grains in the region.

Subject headings: H II regions — ISM: individual (Orion Nebula) — ISM: magnetic fields

On-line material: color figure

1. INTRODUCTION

The Orion complex is one of the best-studied regions of active star formation. These studies include a wide variety of observations of the magnetic field on many angular scales (e.g., van der Werf et al. 1993; Heiles 1997). Star formation is controlled by a complex and dynamic interplay between gravitational, thermal, and magnetic forces. Magnetic effects, in particular, can be complex, yet they must be considered if we are to achieve a comprehensive understanding of the star formation process.

The Orion region consists of ionized (H^+), atomic (H^0), and molecular gas. The H II region is mainly the illuminated face of the background molecular cloud, Orion molecular cloud 1 (see the comprehensive review by O'Dell 2001). It is heated and ionized by the light of the Trapezium cluster, with the single O6 V star θ^1 Ori C (Walborn & Panek 1984) providing most of the energy. The "veil" is the layer of largely atomic gas that lies between the Trapezium and us. Reddening within the H II region itself is small (O'Dell 2002). In addition, optical obscuration toward the nebula correlates well with H^0 column density in the veil (O'Dell & Yusef-Zadeh 2000). Therefore, nearly all obscuration toward the H II region occurs within the veil. Moreover, studies of stellar extinction as a function of distance establish that the veil is associated with the Orion complex (Goudis 1982, p. 38).

A wealth of observational data reveals physical properties of the veil. In particular, the veil is one of the few interstellar regions where we have accurate *maps* of the line-of-sight component of the local magnetic field (Troland et al. 1989). These magnetic field maps are derived from Zeeman splitting of the 21 cm H I line, seen in absorption against the H II region continuum emission. Other physical properties of the veil, such as density, temperature, and level of ionization, can be determined by combining optical and UV absorption-line measurements with photoionization calculations. Altogether, these data present a unique opportunity to test modern theories of the physical state of the interstellar medium (ISM) in star-forming regions.

Section 2 summarizes what is known about the physical state of gas in Orion's veil. Section 3 compares these observations with simulations of the expected thermal and ionization equilibrium. In § 4 we discuss the significance of the model results to magnetic energy equipartition in the veil, and in § 5 we summarize our conclusions.

2. OBSERVED PROPERTIES OF THE VEIL

2.1. *Column Densities and Extinction*

Observations of absorption lines reveal the column densities of a number of atomic and molecular species in the veil. Shuping & Snow (1997, hereafter SS97) derive the atomic hydrogen column density, $N(H^0)$, from *IUE* observations of the Lyα line. Their value of $N(H^0) = (4 \pm 1) \times 10^{21}$ cm^{-2} is a factor of $\sim$4 larger than the previous *OAO 2* and *Copernicus* measurements (Savage & Jenkins 1972; Savage et al. 1977). Column densities of other species were also measured by SS97. Among the most important for this study are the excited states of C^0, O^0, and Si^+. Since the populations of more than one excited state have been measured for each, they can be used as density indicators. The atomic and singly ionized column densities of C, Mg, and S were also measured, and this information constrains the ionization state of the veil. We assume that the physical properties of the gas within the veil are driven by the radiation emitted by the nearby Trapezium stars.

Reddening and extinction to the Trapezium stars and over the entire H II region have been measured by a number of authors (Bohlin & Savage 1981; Cardelli et al. 1989; O'Dell & Yusef-Zadeh 2000). The color excess $E(B-V) = 0.32$ mag,

[1] Department of Physics and Astronomy, University of Kentucky, Lexington, KY 40506; npabel2@uky.edu, gary@pa.uky.edu, gshaw@pa.uky.edu, troland@pa.uky.edu.

[2] Institute for Astronomy, 640 North A'ohoku Place, Hilo, HI 96720; JCMT Fellow; cbrogan@ifa.hawaii.edu.

[3] Department of Physics and Astronomy, Vanderbilt University, Box 1807-B, Nashville, TN 37235; cr.odell@vanderbilt.edu.

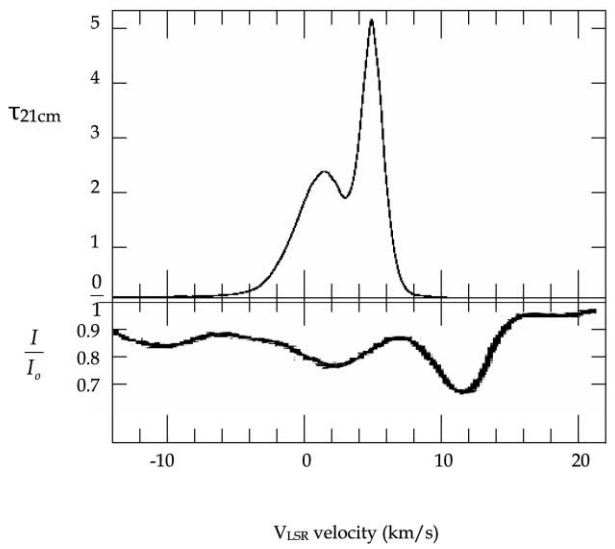

FIG. 1.—H I 21 cm (*top*) and Ca II (*bottom*) profiles observed along the line of sight to the central regions of Orion. The 21 cm profile has optical depth on the *y*-axis, while the Ca II profile is in units relative to the continuum. Note that there does not seem to be a strong correlation between the two profiles, implying that Ca^+ is not associated with the bulk of the material in the veil.

and the extinction $A_V = 1.6$ mag. Therefore, the ratio of total to selective extinction $R = 5.0$, significantly larger than the average value of 3.1 in the diffuse ISM. The high value of R suggests that the reddening is caused by grains with a larger than normal size distribution. The measured visual extinction and the SS97 value for $N(H^0)$ yield a ratio, $A_V/N(H^0)$, of $(4 \pm 1) \times 10^{-22}$ mag cm^2. This value is slightly lower than the average ratio in the diffuse ISM (5.3×10^{-22} mag cm^2), and it is also consistent with larger than normal grains. If any ionized hydrogen is present in the veil, the ratio of visual extinction to total hydrogen column density will be even smaller.

The line of sight to the Trapezium has a surprisingly low fraction of molecular gas. *Copernicus* observations established that $N(H_2) < 3.5 \times 10^{17}$ cm^{-2} (Savage et al. 1977). This value implies $N(H_2)/N(H^0) \lesssim 10^{-4}$ (other regions within the Orion complex are molecular, of course). However, the observed correlations between $N(H_2)/N(H^0)$ and A_V (Savage et al. 1977) suggest that the veil should be predominantly molecular. This anomaly has long been thought to arise from the veil's abnormal grain properties (SS97), although a high UV flux has also been suggested (Savage et al. 1977). Larger grains are less effective at producing H_2, since the grain surface area per unit grain mass is smaller. In addition, large grains are less effective in shielding H_2 from photodissociation by the Lyman-Werner bands because of the smaller projected area per unit mass. The observed $N(H^0)$ and the absence of H_2 in the veil (toward the Trapezium stars) are important constraints on the model calculations presented in § 3.

2.2. 21 cm H I *Velocity Components*

Van de Werf & Goss (1989) reported at least three separate velocity components in the 21 cm H I absorption lines seen against the background H II region. More recent observations of these same 21 cm lines were carried out by T. H. Troland et al. (2004, in preparation) with the Very Large Array of the NRAO[4] and are presented in Figure 1. This line profile reveals two relatively narrow components toward the Trapezium and possibly a broader underlying component. For the purposes of this analysis, we fitted the Troland et al. H I optical depth profile with just two Gaussian components. Inclusion of the underlying broad component does not alter the analysis below in any significant way. Of the two components in the fit, the "narrow" component has V_{LSR} and ΔV_{FWHM} equal to 5.3 and 2.0 km s^{-1}, respectively, and the "wide" component has V_{LSR} and ΔV_{FWHM} equal to 1.3 and 3.8 km s^{-1}, respectively. (Add 18.1 km s^{-1} to convert LSR to heliocentric velocities.) If the line widths result from thermal broadening alone, kinetic temperatures are 87 and 315 K in the narrow and wide components, respectively. However, 21 cm H I lines are almost always broader than thermal, indicating the presence of supersonic motions (Heiles & Troland 2003). Therefore, actual kinetic temperatures may be significantly less.

2.3. *Optical Velocity Components*

For reference, a schematic geometry of the central regions of Orion, based on O'Dell et al. (1993), is shown in Figure 2. Line profiles can be used to reveal kinematics of the various regions. The SS97 UV data had insufficient spectral resolution to resolve lines into individual components. However, the much higher resolution optical study performed by O'Dell et al. (1993) detected many components in the Ca II absorption line toward the Trapezium stars (θ^1 Ori A, B, C, and D) and toward θ^2 Ori. The Ca II profiles for Ori A–D have an absorption component in the same velocity range as the 21 cm H I absorption. (Ca II and 21 cm H I lines are shown in Fig. 1.) However, the Ca II profile has other components not seen in 21 cm H I absorption.

The lack of a strong correlation between Ca II and 21 cm H I absorption profiles may have a simple explanation. The Ca^+ column densities measured by O'Dell et al. (1993) show little variation, ranging from 10.7 to 12.9×10^{11} cm^{-2}. For a gas phase Ca/H abundance of 2×10^{-8} (Baldwin et al. 1991), the associated H^0 column density is 6×10^{19} cm^{-2}. This value is less than 2% of the $N(H^0)$ measured by SS97. Therefore, Ca^+ is a trace constituent within the veil. Photoionization calculations presented below confirm this conclusion. We believe H^0 samples most of the matter in the veil, so we focus on this species in our calculations.

2.4. *Physical Location, Size, and Geometry*

Statistical arguments suggest that the veil is ~0.6 pc away from θ^1 Ori C. This estimate is based on the three-dimensional distribution of stars in the Orion Nebula cluster given by Hillenbrand & Hartmann (1998) and on observations of the fraction of proplyds that are protected by the veil from photoionization and seen in silhouette (Bally et al. 2000). The uncertainty of this value is difficult to estimate.

Another constraint on the veil location comes from the fact that the veil emission in Hβ is not prominent compared to the Hβ surface brightness of the background H II region (5×10^{-12} ergs s^{-1} cm^{-2} arcsec^{-2}; Baldwin et al. 1991). This constraint requires the veil to be much farther away from the Trapezium stars than the main photoionized region (~0.25 pc; Fig. 2). Since the veil's position is poorly constrained by these arguments, we treat it as a free parameter.

[4] The NRAO is a facility of the National Science Foundation operated under cooperative agreement by Associated Universities, Inc.

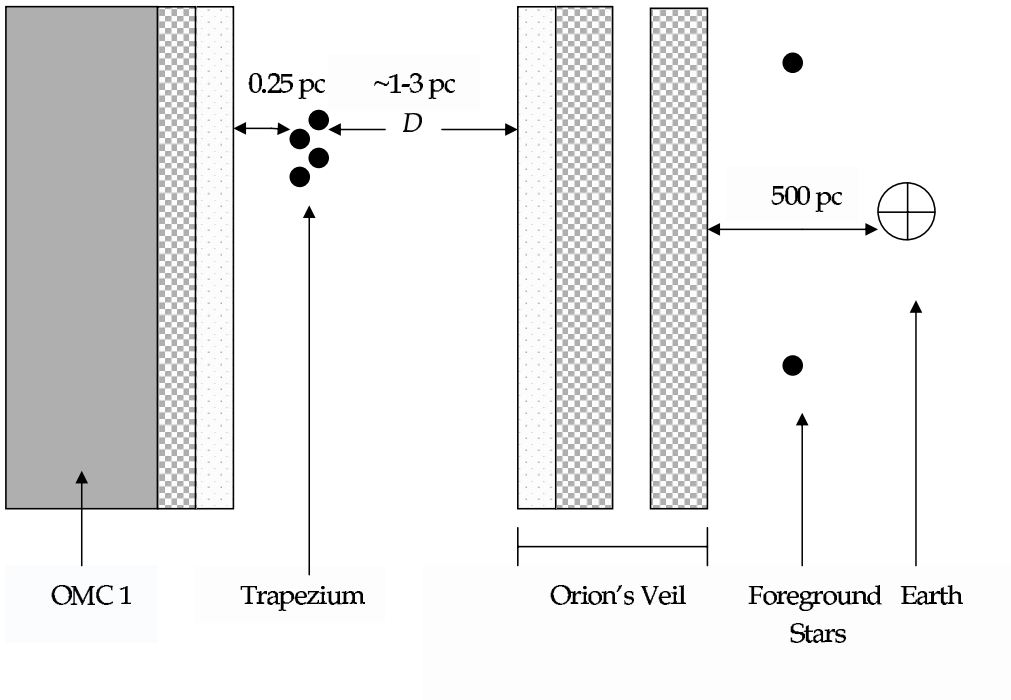

FIG. 2.—Geometry of the central regions of the Orion Nebula and the veil. For this figure, solid regions correspond to H_2, checkered regions to H^0, and dotted regions to H^+. Starting with the side of the veil facing the Trapezium, we have a small H^+ zone followed by a PDR. Because of the strong UV flux coming from the Trapezium cluster, H_2 never readily forms, but instead we have a thick region of atomic hydrogen. The segmented regions in the veil represent the multiple components seen in the 21 cm optical depth profile in Fig. 1. The distance D represents the distance from the side of the veil facing the Trapezium to the Trapezium itself and is the same distance used in all subsequent contour plots. [*See the electronic edition of the Journal for a color version of this figure.*]

The geometric properties of the veil and its density are partly constrained by observational data. The veil subtends at least 10′ in the plane of the sky, since it covers both M42 and M43 (van der Werf & Goss 1989). This dimension amounts to 1.5 pc at 500 pc. The thickness L can be deduced from the SS97 H^0 column density if the atomic hydrogen density $n(H^0)$ is also known, since $L \sim 4 \times 10^{21}/n(H^0)$ cm. If the veil extends no more than ~1.5 pc in the plane of the sky, then this relation sets a lower limit to the density, $n(H^0) > 10^2$ cm^{-3}, since the veil is probably not cigar-shaped and pointed in our direction. There is no real physical upper limit to the density. If $n(H^0) \geq 10^3$ cm^{-3}, then the veil is a sheet viewed face-on. Such sheetlike structures are commonly seen in the diffuse ISM (Heiles & Troland 2003).

2.5. *Harmonic Mean Temperature of* H^0

The 21 cm H I and Lyα data establish the harmonic mean temperature of the veil (see § 3.3). The 21 cm absorption measures $N(H^0)/T_{spin}$ because of the correction for stimulated emission (Spitzer 1978, eqs. [3]–[37]). From the 21 cm data of van der Werf & Goss (1989), $N(H^0)/T_{spin} = 4.3 \times 10^{19}$ cm^{-2} K^{-1} toward the Trapezium stars (integrated across the full line). This value and the measured $N(H^0)$ from SS97 imply a harmonic mean spin temperature of 70–120 K [corresponding to the lower and upper limits to $N(H^0)$ derived by SS97]. However, the narrow H I component must have $T < 87$ K, the temperature equivalent of its full width.

Harmonic mean H^0 temperatures, estimated from Lyα and 21 cm data, are only accurate if both data sets sample the same absorbing gas. This assumption need not be correct, since the Lyα and 21 cm data sample very different projected areas through the veil (subarcseconds for the UV vs. ~15″ for the radio). However, maps of optical extinction suggest it is fairly smooth across the veil (O'Dell & Yusef-Zadeh 2000), so the Lyα and 21 cm data likely sample comparable regions.

2.6. *Magnetic Properties*

Using the Zeeman effect in the 21 cm absorption lines, Troland et al. (1989; T. H. Troland et al. 2004, in preparation) measure line-of-sight magnetic field strengths B_{los} independently in the narrow and wide H I velocity components. Across much of the veil, they find comparable values for the two components, typically -50 μG, where the minus sign indicates a field pointed toward the observer. Along the line of sight to the Trapezium, $B_{los} = -45 \pm 5$ and -54 ± 4 μG for the narrow and wide components, respectively. For a statistical ensemble of randomly directed fields of the same strength, the average total field strength is $2B_{los}$. Therefore, toward the Trapezium stars, we take the total field strength to be -100 μG in the veil.

Field strengths this high are almost exclusively associated with regions of massive star formation, where $n > 10^3$–10^4 cm^{-3} (Crutcher et al. 1999). They are never seen in the diffuse, absorbing H I gas of the cold neutral medium studied by Heiles & Troland (2003), nor are they commonly found in molecular clouds associated with low- and intermediate-mass star formation (Crutcher et al. 1993; Troland et al. 1996). High field strengths in the veil almost certainly reflect the history of this layer, a history associated with a large, self-gravitating region of massive star formation rather than with more typical diffuse ISM.

Equipartition between the (nonthermal) kinetic energy in MHD waves and the energy in the magnetic field is thought to arise commonly in the ISM (Zweibel & McKee 1995). In addition, such equipartition is consistent with observations of regions where magnetic field strengths have been measured

TABLE 1
BEST-FIT PARAMETERS FOR THE VEIL

Parameter	Model[a]	Observed 1 σ range[a]	Reference
n_H (cm^{-3})	$10^{3.1}$	...	...
T_{spin} (K)	68	70–120	1, 2
Distance to θ^1 Ori C (pc)	1.91	~1.0	3
$S(H\beta)$ (ergs s^{-1} cm^{-2} $arcsec^{-2}$)	4.3×10^{-14}	$<5 \times 10^{-12}$	3
S([N II] λ6583) (ergs s^{-1} cm^{-2} $arcsec^{-2}$)	7.3×10^{-14}	$<1.49 \times 10^{-13}$	4
N(C I*)/N(C I)	−0.3	~−0.1	1
N(C I**)/N(C I)	−0.6	~−0.2	1
N(O I*)/N(O I)	−3.0	-3.5 ± 0.7	1
N(O I**)/N(O I)	−4.2	-3.4 ± 0.7	1
N(Si II*)/N(Si II)	−2.2	-1.4 ± 0.4	1
$N(C^0)/N(C^+)$	−4.0	>−4.35	1
$N(Mg^0)/N(Mg^+)$	−3.0	-3.4 ± 0.5	1
$N(S^0)/N(S^+)$	−4.5	$\sim -4.2 \pm 1.0$	1
$N(H_2)$ (cm^{-2})	3.3×10^{14}	$<3.5 \times 10^{17}$	5
$N(H^+)$ (cm^{-2})	1.2×10^{20}	Unknown	...

[a] Ratios are in logarithmic units.

REFERENCES.—(1) Shuping & Snow 1997; (2) van der Werf & Goss, 1989; (3) Baldwin et al. 1991; (4) O'Dell & Yusef-Zadeh 2000; (5) Savage et al. 1977.

(Myers & Goodman 1988; Crutcher et al. 1999). If equipartition exists between magnetic field energy and the energy of nonthermal motions in the gas, then we can express the gas density in terms of the field strength B and the contribution to the line width from nonthermal motions Δv_{NT}. Equating the magnetic field energy with the energy of nonthermal motions,

$$\frac{B^2}{8\pi} = \frac{1}{2}\rho \Delta v_{NT}^2, \quad (1)$$

we find, upon appropriate units conversion,

$$n_{eq} = \left(\frac{2.5B}{\Delta v_{NT}}\right)^2 \text{ cm}^{-3}. \quad (2)$$

Here n_{eq} is the equipartition *proton* density $[n(H^0) + 2n(H_2)]$, B is in μG, and Δv_{NT} is the FWHM line width attributable to nonthermal motions in the gas (km s^{-1}). If $n/n_{eq} > 1$, nonthermal kinetic energy dominates. If $n/n_{eq} < 1$, magnetic energy dominates, and the field lines should be relatively uniform.

3. PHOTOIONIZATION CALCULATIONS

3.1. *The Density-Distance Grid*

Our goal is to deduce the density of the veil and its distance from the Trapezium stars by comparing photoionization models of this layer with observations. We used the development version of the spectral synthesis code Cloudy, last described by Ferland (2002). Bottorff et al. (1998) and Armour et al. (1999) provide further details about this code.

Our veil models incorporate several important improvements in Cloudy. We use the improved grain physics described by van Hoof et al. (2001) that explicitly solves for the grain temperature and charge as a function of grain size. We divide the grain-size distribution into 10 size bins and include grains that are composed of graphite and silicates. Our size distribution is designed to reproduce the flat UV extinction curve observed by Cardelli et al. (1989) toward Orion. We see below (§ 3.4, Table 1) that the best-fit models predict that about 5%–10% of the hydrogen along the line of sight to the Trapezium is ionized and so is not seen in H^+ absorption-line studies. This result, combined with the neutral column density measurements of SS97, makes $A_V/N(H_{tot})$ about 3.5×10^{-22} mag cm^2, a ratio that is ~65% of that seen in the general ISM. We scaled our grain abundance to match this ratio.

We have implemented a complete model of the H_2 molecule in Cloudy. Energies and radiative transition probabilities for the 301 rotational/vibrational levels within the ground electronic state $1s\,^1\Sigma_g$ (denoted as X) are taken from P. Stancil (2002, private communication) and Wolnievicz et al. (1998). We have included the rotational/vibrational levels within the six lowest electronic excited states that are coupled to the ground electronic state by permitted electronic transitions. Energies and radiative transition probabilities for excited electronic states are from Abgrall et al. (2000). These electronic excited states are important because they determine the Solomon process, which destroys H_2 through the absorption of Lyman-Werner band photons from the ground electronic state followed by decays into the X continuum. These photoexcitations are also an indirect source of the population of excited rotational/vibration levels within X that decay to produce infrared emission lines with the selection rule $\delta J = 0, \pm 2$. We have taken photoionization cross sections for transitions into the continuum of the Lyman and Werner bands from Allison & Dalgarno (1969). Effects of cosmic rays and the X-ray continuum are included as well. H_2 can be formed either on dust grains in a cold, dusty environment or from H^- in a hot, dust-free environment. The state-specific (v and J resolved) formation rates of H_2 on grain surfaces and via the H^- route have been taken from Cazaux & Tielens (2002), Takahashi & Uehara (2001), and Launay et al. (1991). Line overlap and self-shielding are also considered. In addition, our calculations are designed to reproduce the observationally determined H_2 formation rate on grains in the diffuse ISM, determined by Jura (1974) to be $\sim 3 \times 10^{-17}$ cm^{-3} s^{-1}.

Other important input parameters to the models include gas-phase abundances and the adopted stellar ionizing continuum. We use the gas-phase abundances observed in the Orion Nebula (Rubin et al. 1991; Osterbrock et al. 1992;

Baldwin et al. 1991). A few of the abundances by number are $He/H = 0.095$, $C/H = 3.0 \times 10^{-4}$, $N/H = 7.0 \times 10^{-5}$, $O/H = 4.0 \times 10^{-4}$, $Ne/H = 6.0 \times 10^{-5}$, and $Ar/H = 3.0 \times 10^{-6}$. However, all of the 30 lightest elements are included in our models. The stellar ionizing continuum is the modified Kurucz LTE atmosphere described by Rubin et al. (1991), which was modified to reproduce high-ionization lines seen in the H II region. We set the total number of ionizing photons emitted by θ^1 Ori C equal to $10^{49.34}$ s^{-1}, a typical value for an O6 star (Osterbrock 1989). The radiation field falls off as the inverse square of the separation from the star, so the star-veil separation becomes a model parameter. Finally, the ionization and thermal effects of background galactic cosmic rays are included using the ionization rate quoted by McKee (1999).

We computed a large grid of models in which two parameters were varied. These parameters are the veil's total hydrogen density, denoted by $n_H = n(H^+) + n(H^0) + 2n(H_2)$, and the distance between the side of the veil facing the Trapezium and the Trapezium itself, which is designated by D. For simplicity we assume a single constant-density layer. This is a reasonable assumption, since the predicted gas temperatures depend on the shielding of the layer from the radiation field, not on the details of how this shielding occurs. All calculated models have the total atomic hydrogen column density measured by SS97, $\log [N(H^0)] = 21.6$. From our results we were able to identify ranges of densities and distances that reproduce the observed features of the veil. A more thorough description of our results is described immediately below.

3.2. *Column Densities, Ionization Structure, and Depletion*

SS97 derived the column densities of many species in the veil in addition to H^0. These results, along with the upper limit to the H_2 column density, allow us to constrain the level of ionization, density, and to some extent the distance from the Trapezium cluster of the veil. Our primary focus here is on column densities for species with more than one stage of ionization. These include atomic and singly ionized C, Mg, and S. Column density ratios of different ion states of the same element determine the level of ionization in a way that does not depend on the abundance. These data determine the ionization parameter: the ratio of the flux of ionizing photons to the density. SS97 derived the column densities of many more elements (such as Fe, Zn, and P), but they were detected in only one stage of ionization. Therefore, these column densities do not constrain the model, since we could easily reproduce them by simply scaling the abundances. The column densities of excited-state O^0, C^0, and Si^+ have also been measured. The ratio of the column densities of the excited to ground state determines the density if the density is less than the critical density of the species. If the density is known, then the measured ionization parameter can be used to determine the distance from the continuum source. The measured column densities are summarized in Table 1.

Model grids for species with more than one observed ionization or excitation state are shown in Figures 3 and 4. Figure 3 shows our predicted ratios of Mg^0/Mg^+, S^0/S^+, and C^0/C^+. There is a large range of parameters that match the observations. All regions that produce $N(Mg^0)/N(Mg^+) < 10^{-3}$ are also consistent with the observed ratios $N(S^0)/N(S^+)$ and $N(C^0)/N(C^+)$. The parameter space with large distances and densities predicts these species to be mostly atomic and is therefore excluded. Figure 4 shows the predicted ratios of the excited to ground state column densities for the five

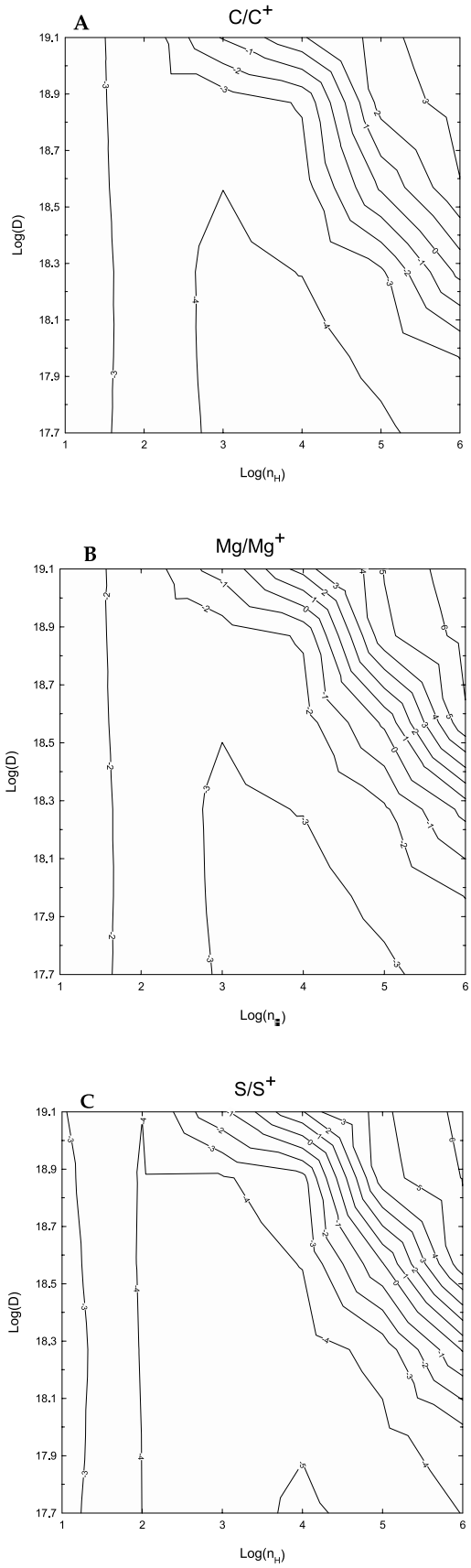

FIG. 3.—Log of the ratio of atomic to ionized (*a*) C, (*b*) Mg, and (*c*) S, which correspond to the column densities measured in more than one stage of ionization by SS97. The observed 1 σ ratios of C (>-4.35), Mg (-3.4 ± 0.5), and S (-4.2 ± 1.0) agree with most of our calculations. In this and all subsequent contour plots, the parameter $n_H = n(H^+) + n(H^0) + 2n(H_2)$ (cm^{-3}), the total hydrogen density in all forms.

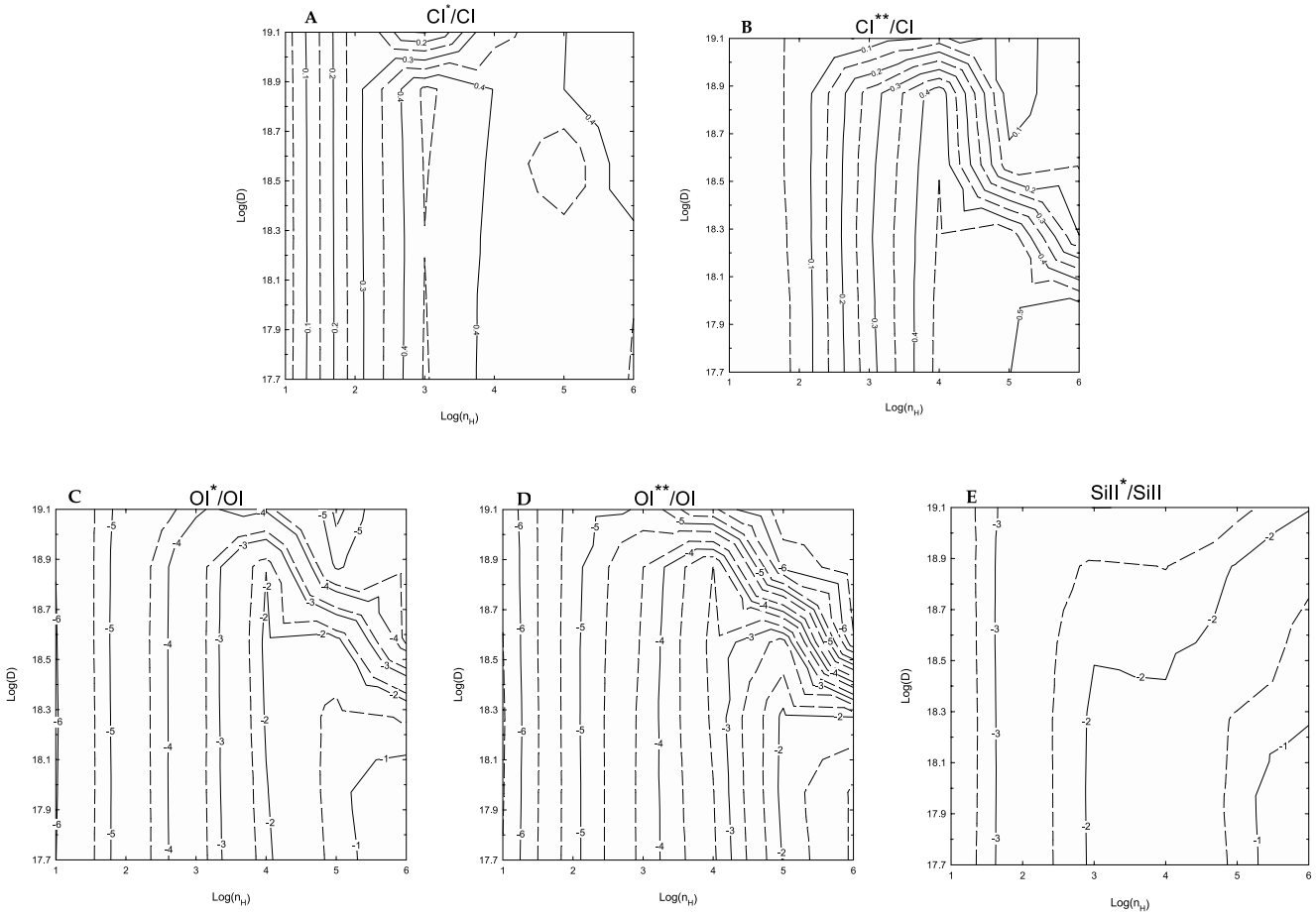

FIG. 4.—Ratio of the excited-state column densities of (*a*, *b*) C, (*c*, *d*) O, and (*e*) Si^+ relative to the ground state. The observed values, with 1 σ ranges when available, are $N(\text{C I}^*)/N(\text{C I}) \sim -0.1$, $N(\text{C I}^{**})/N(\text{C I}) \sim -0.2$, $N(\text{O I}^*)/N(\text{O I}) \sim -3.5 \pm 0.7$, $N(\text{O I}^{**})/N(\text{O I}) \sim -3.4 \pm 0.7$, and $N(\text{Si II}^*)/N(\text{Si II}) \sim -1.4 \pm 0.4$. The parallel contours show their usefulness as density indicators.

species measured by SS97. As expected, these ratios are very sensitive to the hydrogen density. Our calculations reproduce the $N(\text{C I}^*)/N(\text{C I})$ and $N(\text{C I}^{**})/N(\text{C I})$ ratios to within a factor of 2 for densities greater than 10^3 cm^{-3}. Observational uncertainties were not stated for these column densities. The $N(\text{O I}^*)/N(\text{O I})$ and $N(\text{O I}^{**})/N(\text{O I})$ column density ratios are a better constraint in the models since, as for Mg, 1 σ error bars are given. The 1 σ ranges are given in Table 1. The $N(\text{O I}^*)/N(\text{O I})$ ratio suggests $n \sim 10^{3\pm0.4}$ cm^{-3}, while the $N(\text{O I}^{**})/N(\text{O I})$ ratio suggests a density closer to $10^{3.7\pm0.5}$ cm^{-3}. The $N(\text{Si II}^*)/N(\text{Si II})$ ratio gives $n = 10^{4.5\pm0.5}$. A density of $n \sim 10^3$ cm^{-3} matches the observed column densities within 3 σ.

Both the H_2 formation and destruction physics are included in a self-consistent manner. We show in Appendix A that the predicted H_2 column density is very sensitive to the method used in calculating the Solomon process. We also show in Appendix A the sensitivity of the predicted H_2 column densities to the grain-size distribution. We find that the lack of H_2 in the veil is due to the efficiency of the Trapezium stars in destroying H_2 and to the sensitivity of molecular hydrogen formation to the grain-size distribution. The continuum radiation responsible for the Solomon process is mainly the high-energy range of the Balmer continuum, between 11.2 and 13.6 eV. The right axis of Figure 5 gives G_0, the average interstellar flux between 6 and 13.6 eV as defined in Tielens & Hollenbach (1985, hereafter TH85), for the range of distances we consider. Its large value ($G_0 > 10^3$) leads to most of our calculated H_2 column densities being well under the *Copernicus* limit of $N(H_2) < 3.5 \times 10^{17}$ cm^{-2}. Generally, only in regions of parameter space of higher density, farther away from the ionizing star ($D \sim 10^{19.0}$ cm), does G_0 become small enough for a large amount of H_2 to form.

Figure 5 can be used to derive a constraint to the distance D if the density $n_{\rm H}$ is known. Section 3.4 shows that the range of densities that best reproduce observations is $\sim 10^3$ cm^{-3} $< n_{\rm H} < 10^4$ cm^{-3}. Since the H_2 column density must be less than the upper limit derived by *Copernicus*, $N(H_2) < 3.5 \times 10^{17}$ cm^{-2}, our models constrain D to be less than 3 pc.

3.3. *The Spin Temperature and Surface Brightness*

The temperature measured by the 21 cm/Lyα ratio is an $N(H^0)$-weighted harmonic mean temperature, given by the relationship

$$\frac{1}{\langle T_{\rm spin} \rangle} = \frac{\int n/T_{\rm spin}\, dr}{N(\text{H}^0)}. \tag{3}$$

The predicted values are shown in Figure 6. Like the excited-state column densities, the spin temperature is sensitive to the density. For our calculations, the primary heating and cooling mechanisms are the grain photoionization and collisional excitation, respectively, of heavy-element fine-structure lines. The two most efficient coolants were the [C II] 158 μm and the [O I] 63 μm lines. For lower densities, both [C II] and [O I] contribute to the cooling. However, for densities larger

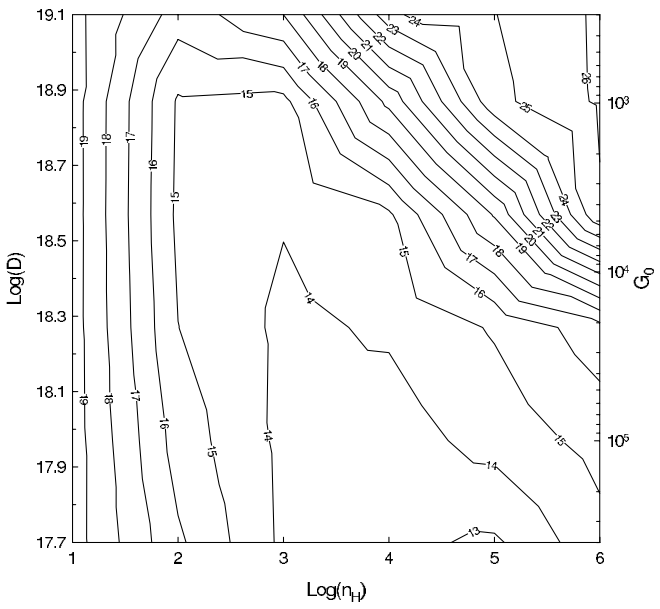

FIG. 5.—Log of the predicted H_2 column density (cm^{-2}). *Copernicus* observations set an upper limit of $N(H_2) < 3.5 \times 10^{17}$ cm^{-2} ($\log [N(H_2)] < 17.55$). In addition to distance, on the right the scale is in units of the average UV radiation field (TH85). For the range of densities that our calculations predict for the veil (10^3–10^4 cm^{-3}), our calculations also predict an H_2 column density less than the *Copernicus* upper limit for distances less than $\sim 10^{19.0}$ cm. For very low densities, the large thickness of the H^+ region causes the value of G_0 to decrease because of geometrical dilution. By the time the hydrogen becomes atomic at these low densities, G_0 has decreased to 1 Habing for all distances. This is why the contours are vertical at low density.

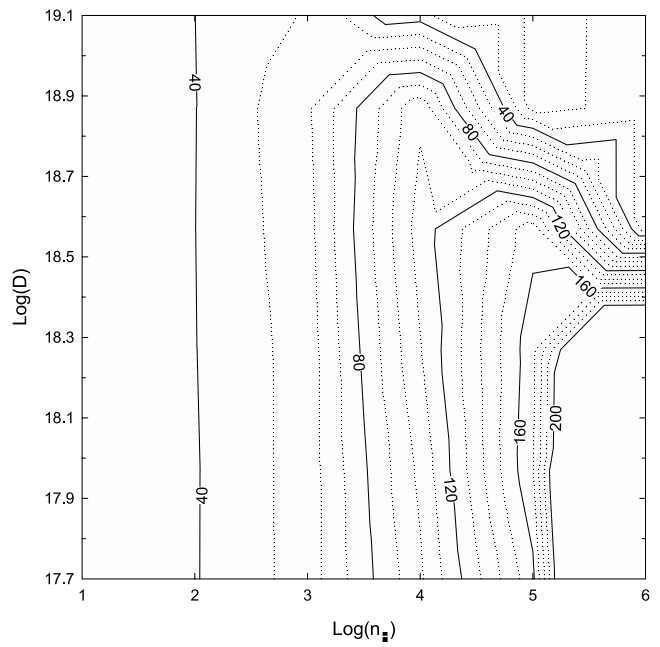

FIG. 6.—Predicted H I spin temperature (K). For densities less than the critical density of [C II] 158 μm (3×10^3 cm^{-3}), the temperature remains relatively constant. However, for densities greater than this, [C II] is no longer an efficient coolant, and the heating rate increases with a power of density greater than that for the cooling. The upper left corner corresponds to calculations that have a large abundance of molecules.

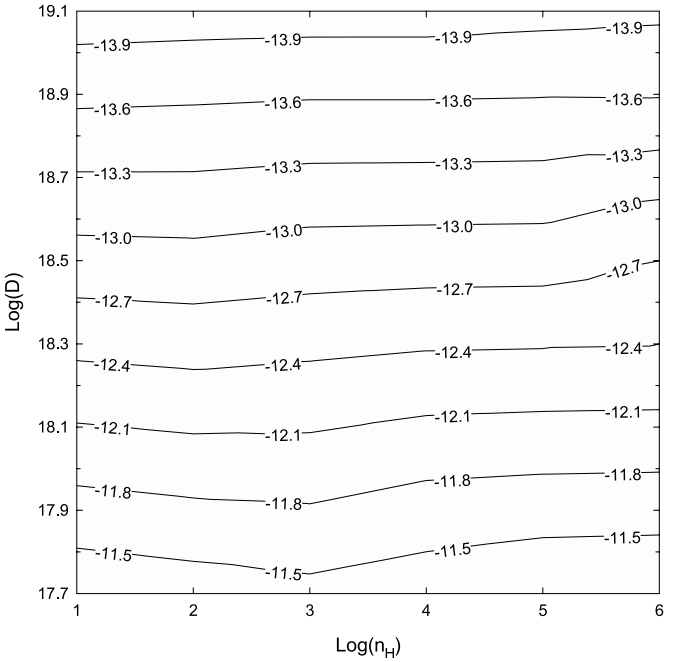

FIG. 7.—Log of the predicted Hβ surface brightness (ergs cm^{-2} s^{-1} $arcsec^{-2}$). The parallel horizontal contours are expected, given the inverse square relationship of surface brightness with distance. The actual surface brightness must be substantially smaller than the total observed surface brightness of 5×10^{-12} ($\log [H\beta] = -11.3$), which mainly comes from the main ionization front.

than the [C II] 158 μm critical density of $\sim 3 \times 10^3$ cm^{-3}, cooling becomes less efficient, and the heating rate increases with a power of density greater than the cooling rate. This explains the increase in temperature seen in Figure 6 for densities greater than 10^3 cm^{-3}. For the 1 σ range of the spin temperature set by the observed 21 cm/Lyα limit, $70 \text{ K} < T_{\rm spin} < 110$ K, our predictions agree with observations for densities between $10^{3.5}$ and $10^{4.5}$ cm^{-3}. The 3 σ range of the spin temperature, 50–200 K, allows densities greater than $\sim 10^2$ cm^{-3}.

Although the veil is known to be deficient in small grains (§ 2.1), we considered the possible effects of polycyclic aromatic hydrocarbons (PAHs) in the model calculations. Very small grains, or large molecules such as PAHs, are known to be very efficient at heating gas. As a check on their effects, we ran one set of models with PAHs present at an abundance of $n(\text{PAH})/n(\text{H}) = 3 \times 10^{-7}$. As expected, the PAHs raised our predicted temperatures by factors between 1.5 and 2 over those shown in Figure 6. The effect of higher temperatures can only be accommodated at lower densities. That is, the models predict slightly lower densities with the inclusion of PAHs. Therefore, the conclusions in § 4 based on relatively low veil densities are not endangered by the effects of PAHs in the models.

Figure 7 shows the predicted Hβ surface brightness emitted by the ionized face of the veil. The contours are very nearly parallel, depending mainly on the distance, since the surface brightness in a recombination line is determined by the flux of ionizing photons striking the gas. Furthermore, the ionizing flux (hence, the Hβ surface brightness) is an inverse square function of the star-cloud distance. If we assume that the surface brightness in the veil is no more than half of that observed in the main ionization front, then a lower limit for the distance from the veil to θ^1 Ori C is $D \sim 10^{18.0}$ cm ($\sim$0.33 pc).

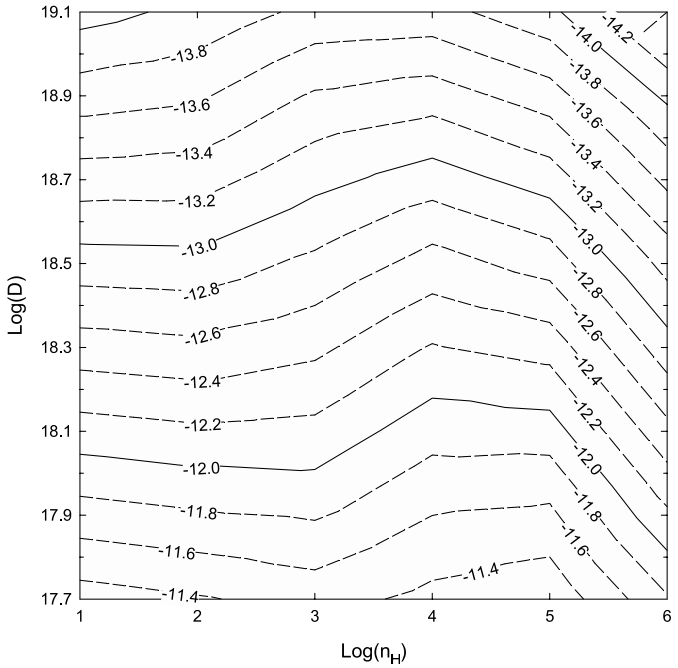

FIG. 8.—Predicted [N II] surface brightness (ergs cm^{-2} s^{-1} arcsec^{-2}). Based on calculations by O'Dell et al. (2003), the upper limit to the veil surface brightness is found to be 1.49×10^{-13} ergs s^{-1} cm^{-2} arcsec^{-2} (-12.8). For the range of densities that our calculations predict are most likely for the veil (10^3–10^4 cm^{-3}), this corresponds to a lower limit to the distance of $\sim 10^{18.5}$ cm.

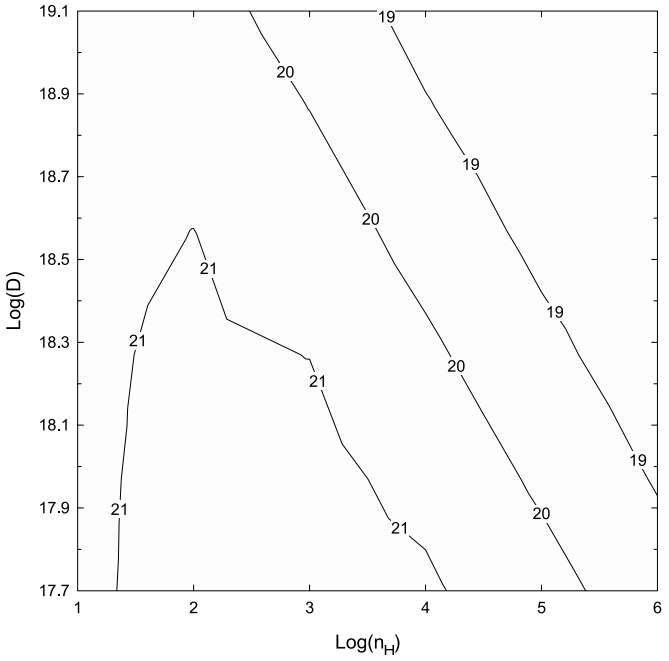

FIG. 9.—Log of the predicted H^+ column density (cm^{-2}). This is sensitive to the ionization parameter, which is the dimensionless ratio of flux to density. As expected, larger distances from the ionizing source (and hence smaller flux) and larger densities combine to lower the ionization parameter and hence the H^+ column density. For our best model, about 5% of the total hydrogen is in the form of H^+.

A firmer lower limit on D can be derived through the use of [N II] λ6583 emission, which must be occurring at the surface of the veil that faces θ^1 Ori C. The difficulty is in distinguishing between veil emission and radiation from the main body of the nebula. An upper limit on the [N II] λ6583 veil emission can be placed by assuming that the veil accounts for the red shoulder of the main nebular emission line. In this case, the surface brightness of the veil is 1.5×10^{-13} ergs cm^{-2} s^{-1} arcsec^{-2} (or about -12.8 on a logarithmic scale), after correction for extinction (O'Dell & Yusef-Zadeh 2000). However, this is a generous upper limit, since it is likely that much of the red shoulder is caused by redshifted nebular light that is scattered by dust in the dense photodissociation region (PDR) that lies beyond the main ionization front of the nebula (O'Dell 2001).

Figure 8 shows the predicted [N II] surface brightness as a function of density and distance. All combinations of density and distance in Figure 8 with [N II] greater than -12.8 (corresponding to contours below the -12.8 contour in Fig. 8) are excluded by observation. For densities less than 10^4 cm^{-3}, this constraint places a lower limit on the distance of $\sim 10^{18.5}$ cm ($\sim$1 pc). Our best models (§ 3.4) calculate $n_{\rm H}$ to be between 10^3 and 10^4 cm^{-3}. Therefore, this upper limit on D applies. The limit $D > 1$ pc is about 2 times larger than the value deduced on statistical grounds (§ 2.4). Since our calculations best match observations for densities between 10^3 and 10^4 cm^{-3}, we are only concerned with the part of Figure 8 that constrains the distance to around 1 pc. As discussed below, our models with $D > 10^{18.5}$ cm also yield the best agreement with the rest of the observational data.

In Figure 9 we present contours of H^+ column density as a function of D and $n_{\rm H}$. For high density and large D, the amount of H^+ starts to drop off. This is due to a lower ionization parameter, defined as the dimensionless ratio of hydrogen ionizing flux to density. This behavior also affects the [N II] surface brightness at high density and large D (Fig. 8). Since nitrogen has a higher ionization potential than hydrogen, nitrogen will only be ionized in regions where hydrogen is also ionized. This leads to less N^+ in these regimes and therefore a lower surface brightness for the 6583 Å line.

3.4. *A "Best Model" for the Veil and Its Consequences*

In this section we define a "best model" that most accurately reproduces the observational features in the veil. Based on our calculations for the excited-state abundance ratios and spin temperatures discussed in §§ 3.2 and 3.3, a density between 10^3 and 10^4 cm^{-3} would reproduce all the observational data to within 3 σ. The distance of the veil, $\sim 10^{18.5}$–$10^{19.0}$ cm (1–3 pc), is set by the observed upper limits on both the surface brightness of [N II] λ6583 and the column density of H_2. These are the broad limits to any successful model of the veil.

We derived a best model using the optimization methods that are part of Cloudy, starting with density and distance near the center of the allowed range but allowed to vary. The observables that we optimized included the column densities of C I, C II, Mg I, Mg II, S I, S II, Si II, O I, Si II*, O I*, O I**, C I*, C I**, and H_2 and the temperature $T_{\rm spin}$. We used as confidence intervals the 1 σ error estimates given by SS97. When these were not given, a 20% error was assumed. Where upper limits were given (as in the case of C^+, S^0, and H_2), all that was required in the calculation was that the predicted column densities be less than these upper limits. We then calculated a χ^2 based on the formula

$$\chi^2 = \left[\frac{F_{\rm obs} - F_{\rm pred}}{\sigma \min\left(F_{\rm obs},\ F_{\rm pred}\right)} \right]^2, \qquad (4)$$

TABLE 2

Log of Column Densities for the Best-fitting Model

Element	Stage of Ionization			
	I	II	III	IV
H	21.6	20.1		
He	20.6	18.8		
Li	7.8	11.3		
Be		1.6		
B	7.5	11.6	8.8	7.0
C	14.1	18.1	15.9	11.0
N	17.4	15.8	15.3	10.5
O	18.2	16.6	15.7	
F	1.6			
Ne	17.4	15.9	14.3	
Na	12.8	15.1	10.3	
Mg	13.1	16.1	14.4	
Al	10.4	14.9	12.8	11.4
Si	11.4	16.2	14.4	12.
P	10.5	14.8	13.0	10.8
S	12.1	16.6	14.9	12.2
Cl	10.4	14.6	12.7	9.4
Ar	16.1	14.3	14.3	10.9
K	11.3	13.6	11.5	7.3
Ca	8.7	11.8	13.9	7.5
Sc		0.2	1.6	
Ti	8.5	12.3	11.8	9.8
V	8.3	11.6	10.0	8.8
Cr	9.5	13.6	12.0	10.6
Mn	11.4	14.0	12.4	10.8
Fe	12.4	16.1	14.4	13.6
Co		1.6		
Ni	11.5	14.6	12.9	11.3
Cu	9.1	12.8	11.2	9.3
Zn	11.0	13.9	12.0	10.0

where F_{obs} is the observed mean value, F_{pred} is the predicted value generated by Cloudy, and σ is the error in the observed value.

Tables 1 and 2 along with Figure 10 summarize our calculation that had the lowest χ^2 and therefore represents our best model of the physical conditions in the veil. The distance is $10^{18.8\pm0.1}$ cm ($\sim$2 pc), and hydrogen density is $n_H = \sim 10^{3.1\pm0.2}$ cm^{-3}, where the ranges correspond to densities and distances that yield a χ^2 that are within a factor of 2 of the lowest value. The general conclusions drawn from our best model are representative of all models in this general range of the parametric diagrams.

Our optimal calculations predict column densities in unobserved stages of ionization. The majority of calcium in the veil is in the form of Ca^{++} (see Table 2, Fig. 10*b*). Doubly ionized calcium has a closed shell and hence is undetectable in UV or optical radiation. Optical studies must work with Ca^{+}, which is a trace stage of ionization. It is for this reason that we take the 21 cm H I absorption line as the principal tracer of atomic gas (§ 2.3). We also predict that about 5% of the hydrogen in the veil is ionized.

Formalized optimization aside, how certain can we be that veil densities are as low as $n_H \sim 10^3$ cm^{-3} (best model) and not $n_H \geq 10^4$ cm^{-3}, as required for magnetic equipartition in the narrow H I component (§ 4.2)? The best determined line ratios (and therefore, the best diagnostics for determining density) are O I*/O I, O I**/O I, Si II*/Si II, and Mg^0/Mg^+ (§ 3.2). Line ratios involving C and S have either undetermined

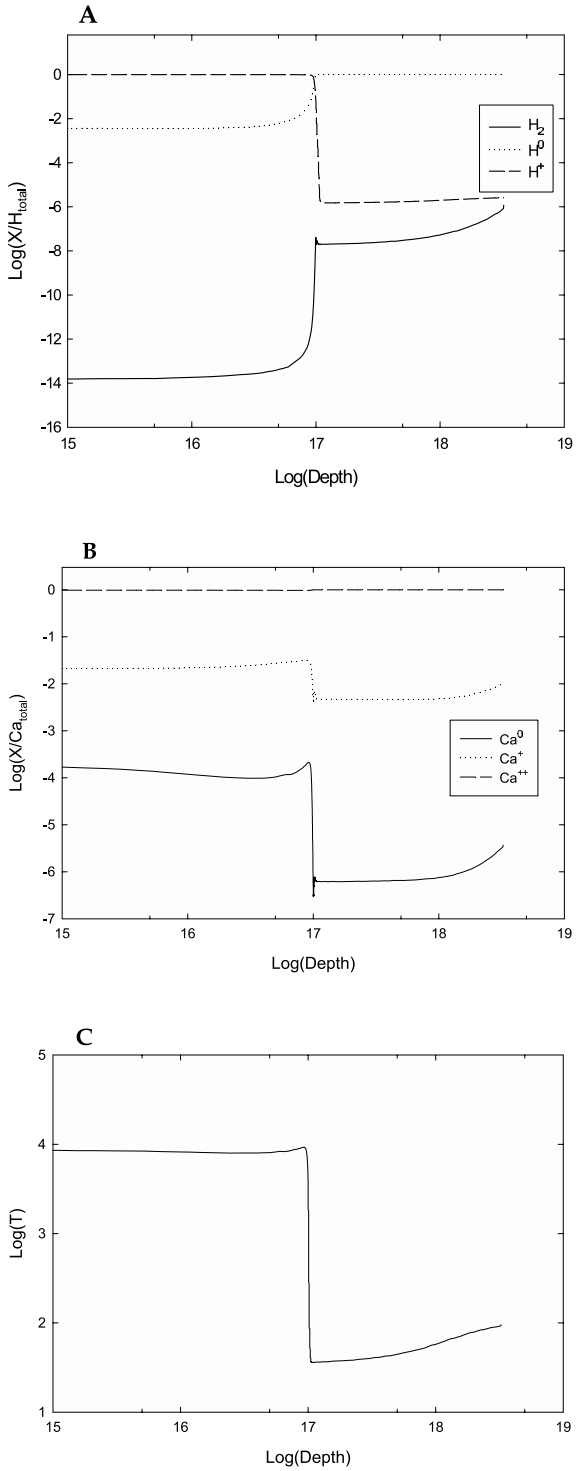

Fig. 10.—Fractional abundances of (*a*) H and (*b*) Ca in various forms as a function of depth (in cm) into the veil for our best model. Also shown is (*c*) the temperature vs. depth into the veil, with the temperature in kelvins. The drop in temperature corresponds to the hydrogen ionization front. Also of note is that our calculations predict the majority of calcium to be in the form of Ca^{++}.

observational errors or else errors too high to be useful (see Table 1). For our optimized density ($n_H = \sim 10^{3.1\pm0.2}$ cm^{-3}), the predicted O I*/O I ratio is within 1 σ of observation. If $n_H \geq 10^4$ cm^{-3}, then the predicted ratio is only within 3 σ of observation. Likewise, the predicted ratio Mg^0/Mg^+ at the optimized density lies within 1 σ of observation, while

the predicted density for $n_{\rm H} \geq 10^4$ cm^{-3} falls only within 3 σ of observation. However, our models do not predict the Si II*/Si II ratio very well at an $n_{\rm H}$ of either $\sim 10^3$ or 10^4 cm^{-3}. For both densities, the predicted ratio barely falls within 3 σ of observation. In addition, the predicted ratio O I**/O I lies within 2 σ of observation at either value for $n_{\rm H}$. In general, our calculations show that densities greater than 10^4 cm^{-3} combined with distances greater than 1 pc (the minimum distance allowed by the [N II] surface brightness measurement) predict the veil to be both less ionized and more molecular than suggested by observation. However, the best case for $n_{\rm H} \simeq 10^3$ cm^{-3}, as opposed to 10^4 cm^{-3}, comes from the ratios O I*/O I and Mg^0/Mg^+ mentioned above.

Future observations of the line of sight toward θ^1 Ori C done at higher spectral resolution could further increase our knowledge of the physical conditions in the veil. Observations in the UV, done at higher resolution than possible for *IUE*, would allow for the determination of the physical properties in each of the veil's components seen in 21 cm H I absorption. In a manner similar to what we have done in this work, excited-state column densities along with column densities of elements seen in more than one ionization state could be calculated for each component in the veil. This information could then be used to derive the density, temperature, and level of ionization for each component in the veil. In addition, observations of H_2 performed with greater sensitivity than that of the *Copernicus* mission could yield a more precise value for the column density of H_2 in the veil.

4. IMPLICATIONS FOR THE MAGNETIC FIELD IN THE VEIL

4.1. *Magnetic versus Nonthermal Energies in the Veil*

Knowledge of the magnetic field strength, gas density, and nonthermal line width in the veil allows us to estimate the energetic importance of the magnetic field. The ratio of energy in nonthermal motions to energy in the field equals $n_{\rm H}/n_{\rm eq}$, the ratio of the actual gas density to the equilibrium density (§ 2.6; densities are proton densities, i.e., densities for H^0). Values of n are inferred from our models, where, for the veil, $n_{\rm H} \approx n(H^0)$. In these models, higher n is associated with higher T_s over a wide range of veil distance d (Fig. 6). A lower limit to $n_{\rm eq}$ comes from equation (2), assuming $\Delta v_{\rm NT} = \Delta v_{\rm obs}$, that is, that the observed line width $\Delta v_{\rm obs}$ has no thermal broadening. For nonzero temperature, $\Delta v_{\rm NT} < \Delta v_{\rm obs}$, and $n_{\rm eq}$ is higher. Therefore, the question of magnetic energy dominance is addressed by estimating the ratio $n_{\rm H}/n_{\rm eq}$ as a function of T_s over the allowable T_s range for the veil. To do so, we make use of the model-determined T_s-$n_{\rm H}$ relationship of Figure 6.

4.2. *The Narrow* H I *Component*

We now consider the ratio $n_{\rm H}/n_{\rm eq}$ for the narrow H I component. The upper limit to T_s is 87 K, set by $\Delta v_{\rm obs}$. Although the harmonic mean temperature of the veil is 70–120 K (§ 2.5), the 21 cm and Lyα data set no lower limit on T_s for the narrow component alone. We have estimated the ratio $n_{\rm H}/n_{\rm eq}$ over the range 0 K $< T_s <$ 87 K. To do so, we used $\Delta v_{\rm obs} = 2$ km s^{-1} and $B = 100$ μG (§ 2.6), implying $n_{\rm eq} \geq 1.6 \times 10^4$ cm^{-3}. We also used the $n_{\rm H}$-T_s relationship in Figure 6 over the range $D = 10^{18.8 \pm 0.1}$ cm of our best models (§ 3.4). At all values of T_s, the ratio $n_{\rm H}/n_{\rm eq} < 0.025$, that is, magnetic energy is greater than the energy of nonthermal motions by at least a factor of 40. Even at the minimum possible $B = B_{\rm los} \approx 50$ μG (§ 2.6), the magnetic energy dominates by an order of magnitude. Note that for $T_s < 87$ K, Figure 6 allows for higher densities ($n_{\rm H} > 10^4$ cm^{-2}) at larger values of D ($>10^{19}$ cm). However, this range of parameter space is excluded by the observed upper limit on $N(H_2)$ as shown in Figure 5. That is, a high-density veil located far from θ^1 C Ori would become largely molecular, contrary to observations. The conclusion seems quite certain that magnetic fields dominate nonthermal motions in the narrow H I component.

It is possible that the field lies nearly along the line of sight, with transverse MHD wave motions nearly in the plane of the sky. In such a case, the measured (line of sight) line width of the narrow component yields an underestimate of the actual nonthermal motions, and hence an underestimate of $n_{\rm H}/n_{\rm eq}$. We regard such an effect as very unlikely. A very high degree of alignment and MHD wave coherence would be necessary to reduce significantly the gas motions along the line of sight compared to those in the plane of the sky.

Such a pronounced dominance of magnetic field energy is unknown anywhere else in the ISM. It is unexpected theoretically and unprecedented observationally (§ 2.6). Dominance by the magnetic field implies that the field should be rather uniform owing to tension in the magnetic field lines (e.g., Chandrasekhar & Fermi 1953). In fact, the magnetic field map across the veil reveals a rather uniform distribution of $B_{\rm los}$, except in the northeast, where $B_{\rm los}$ increases substantially in the direction of the dark bay of obscuring material (T. H. Troland et al. 2004, in preparation). Magnetic dominance and a uniform field might arise if there is little input of mechanical energy to the gas or if the mechanical energy has damped out. Perhaps this is the case in the narrow component. Van der Werf & Goss (1989) identified this component with quiescent gas undisturbed by the H II region. However, Watson et al. (2001) analyzed the statistics of variation of magnetic fields in the Troland et al. data set. They concluded that field variations across the veil were consistent with magnetic equipartition. Such a conclusion seems difficult to reconcile with the present results for the narrow component.

Turbulent line broadening is not necessarily related to MHD waves. For example, O'Dell et al. (2003) argue that the anomalous broadening of 10–20 km s^{-1} observed in optical emission lines from the H II region is not an MHD effect. Conceivably, H^0 gas in the veil may also exhibit nonmagnetic turbulent broadening. However, the veil is known to have a significant magnetic field. Therefore, nonthermal motions in the veil will inevitably be coupled to the field unless magnetic flux freezing is extremely inefficient. Therefore, our assumption that line broadening in the veil is magnetic seems inescapable.

4.3. *The Wide* H I *Component*

A similar assertion of magnetic dominance cannot be made for the wide H I component ($\Delta v_{\rm obs} = 3.8$ km s^{-1}). For this component, $n_{\rm eq} \geq 4 \times 10^3$ cm^{-3} (eq. [2] with $B = 100$ μG and $\Delta v_{\rm NT} = \Delta v_{\rm obs}$). This limit on the equipartition density is comparable to the best-fit model density of $10^{3.1}$ cm^{-3}, so $n_{\rm H}/n_{\rm eq} \approx 1$. In short, parameters for the wide H I component are consistent with magnetic equilibrium in this layer of the veil, so they are consistent with the analysis of Watson et al. (2001).

5. CONCLUSIONS

We have combined radio, optical, and UV data with an extensive series of photoionization models to define better the physical conditions in the veil of Orion. The models have

been computed in a grid in which the density of the veil and its distance from the principal source of ionizing photons, θ^1 Ori C, are treated as free parameters. This study has led to an improved understanding of the location of the veil, its density, its ionization structure (including the atomic and molecular hydrogen content), and the role of the magnetic field within it. Our principal conclusions are summarized below. These conclusions apply to the line of sight through the veil to the Trapezium stars, principally θ^1 Ori C.

1. Model calculations (§ 3) constrain the density in the veil to 10^3 cm$^{-3} \lesssim n_{\rm H} \lesssim 10^4$ cm^{-3}. The models also reveal a monotonic connection between density and temperature: higher temperatures are associated with higher densities for $n_{\rm H} \leq 10^4$ cm^{-3} (Fig. 6). The best-fit model has $n_{\rm H} \sim 10^{3.1}$ cm^{-3} at $T \sim 70$ K.

2. Model calculations place the veil 1–3 pc away from the Trapezium; the best-fit value is 2 pc. In addition, measurements of the surface brightness of [N II] λ6583 require the veil to be at least 1 pc from the Trapezium. These distances are about 2–5 times greater than the 0.6 pc value suggested by previous statistical analyses.

3. Model calculations suggest H_2 is underabundant because of a combination of the high UV flux incident on the veil and the larger than normal grains. In addition, the predicted H_2 abundance is very sensitive to the details describing the dissociation and formation processes (Appendix A). This means that straightforward approximations previously used in calculating the dissociation rate may not accurately predict H_2 abundances in at least some circumstances. In this study, we have used a greatly improved model for the H_2 molecule that incorporates over 10^5 rotational/vibrational levels.

4. The models confirm that Ca^+ is only a trace stage of ionization in the veil. Therefore, studies of Ca II optical absorption profiles may not be representative of most of the matter in the veil. However, 21 cm H I absorption traces all of the matter in the veil except for the small fraction in the form of H^+. Model calculations predict that about 5%–10% of the hydrogen in the veil is ionized.

5. There are two principal velocity components in the 21 cm H I absorption, which we designate as the narrow and the wide components. Magnetic field measurements made via the Zeeman effect (Troland et al. 1989; T. H. Troland et al. 2004, in preparation) reveal the line-of-sight field strength $B_{\rm los}$ across the veil. In the direction of the Trapezium stars, $B_{\rm los} \sim -50$ μG for each of these components, with the total field strength statistically expected to be 2 times larger. We show from model estimates of density in the veil that the narrow H I component is strongly dominated by the magnetic field. That is, the field energy is much larger than the energy associated with nonthermal motions in the gas. The narrow H I component in the veil is the only interstellar environment known with this property.

6. For the derived density of $10^{3.1}$ cm^{-3} and observed column density of $N({\rm H}^0) \approx 10^{21.6}$ cm^{-2}, the physical thickness of the layer is $\approx$1 pc. The veil covers more than 1.5 pc in the plane of the sky, and its aspect ratio is more than 1:1.5, so it is not necessarily a sheet. Were the density high enough to be in energy equipartition, $n \sim 10^4$ cm^{-3}, the veil would be a thin sheet, with an aspect ratio greater than 1:15.

We also would like to thank referee Mark Wolfire for his invaluable suggestions with drafts of this work. G. J. F. thanks the National Science Foundation (NSF) for support through AST 03-07720 and NASA for NAG5-12020. T. H. T. would like to acknowledge the support of NSF grants 99-88341 and 03-07642. Support for C. R. O. was in part from the Space Telescope Science Institute grant GO-9141.

APPENDIX A

SENSITIVITY OF $N(H_2)$ TO FORMATION AND DESTRUCTION RATES

In this section we show the extreme sensitivity that predicted molecular hydrogen column densities have to the formation and destruction rates. In the ISM, molecular hydrogen forms primarily through catalysis of two hydrogen atoms on grain surfaces. Destruction of H_2 occurs through photoabsorption in the Lyman-Werner bands. Calculating formation and destruction rates for the H_2 molecule can be computationally expensive, since the number of rotational/vibrational levels for H_2 is $\sim 10^5$. We refer to the treatment of all levels of H_2 in calculating formation and destruction rates as using the "complete H_2 molecule," as in § 3.2. The population of each level is determined by balancing processes that correspond to formation into it, destruction from it, and transitions to and from other levels.

Often approximations to the formation and destruction rates are made, with the ultimate goal of increasing calculation speed while at the same time making predictions for H_2 abundances to the same level of accuracy as the complete H_2 molecule. Then the chemistry can be treated as a simple two-component system, and the balance can be written as

$$n({\rm H}_2)R_d = \frac{1}{2} n\left({\rm H}^0\right) n R_f \ {\rm cm}^{-3} \ {\rm s}^{-1}, \tag{5}$$

where the photodestruction and grain formation rates are given by R_d and R_f, the stoichiometric factor is $\frac{1}{2}$, and $n({\rm H}^0)$ and n are the atomic and neutral hydrogen densities $[n = 2n({\rm H}_2) + n\left({\rm H}^0\right)]$.

A1. DESTRUCTION RATES

Two widely used approximations to the destruction rates of H_2 come from Bertoldi & Draine (1996, hereafter BD96) and TH85. While these approximations increase computational speed, the true dissociation rate may deviate significantly from simple analytical approximations if the UV field excites electrons to many different rotational/vibrational levels.

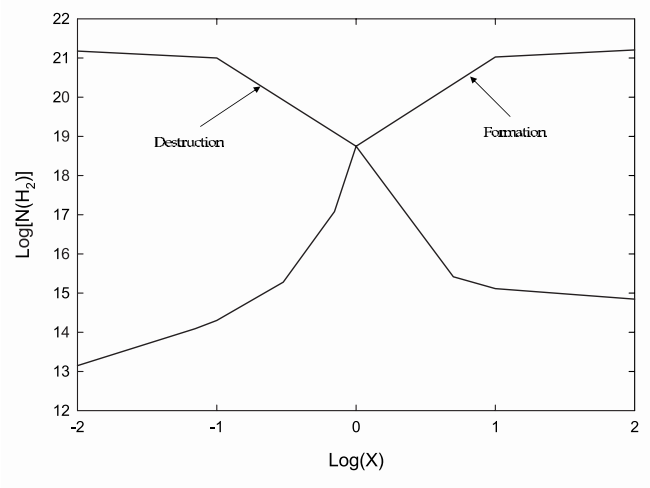

FIG. 11.—Predicted H_2 column density (cm^{-2}) as a function of the dissociation and formation rate scaling factor X. This plot clearly illustrates the sensitivity of the H_2 column density to the various rates. Changes in either rate of an order of magnitude can cause changes to the H_2 column density of up to 6 orders of magnitude. In order to have confidence in predicting the H_2 column density, one must model the H_2 formation and destruction processes as accurately as possible, without resorting to approximations.

We tested how variations in these simple approximations to the destruction rates changed the predicted H_2 column density. First, in the case of destruction, we took the destruction rate given in the TH85 paper and scaled it in the following manner:

$$R_d = X\left(3.4 \times 10^{-11}\right)\beta(\tau)G_0 e^{-2.5A_v}\ \mathrm{s}^{-1}. \tag{6}$$

Here $\beta(\tau)$ is a self-shielding factor that characterizes the amount of the continuum between 6 and 13.6 eV that has been absorbed by the Lyman-Werner bands. As H_2 becomes more shielded from these photons, $\beta(\tau)$ will decrease. The parameter G_0 is the flux of UV photons between 6 and 13.6 eV relative to the average interstellar value, with the exponential factor accounting for dust absorption of photons in the same range of energy. The scale factor X is a free parameter that we use to test how the predicted H_2 column density varies with changes in the destruction rate. The BD96 destruction rate is very similar, with the exception that self-shielding is unity for H_2 column densities less than 10^{14} cm^{-2}, which in terms of equation (5) means that $\beta(\tau)$ varies differently with depth.

As Figure 11 shows, scaling the simple dissociation rate by factors of less than 10 can cause the predicted H_2 column density to change by several orders of magnitude. This sensitivity is due to the nonlinear effects that changes in H_2 have on the self-shielding. Increasing the H_2 destruction rate will decrease the amount of H_2. Consequently, a decreased H_2 abundance will lead to less absorption of the Lyman-Werner bands [a higher $\beta(\tau)$], and hence less self-shielding. This positive feedback mechanism produces the large changes in H_2 abundance for small changes to the scaling factor seen in Figure 11.

One would not expect either the TH85 or BD96 destruction rate to exactly match the H_2 destruction rate generated by Cloudy. Cloudy self-consistently determines the photodestruction rate for each line, including attenuation by absorption, reemission by the gas, and line overlap. This is done for each depth into a cloud. Combining the use of a complete H_2 molecule with a self-consistent treatment of the radiation field gives the most physically realistic treatment of the Solomon process.

We compared the predicted H_2 abundance for three different treatments of the destruction rate, keeping all other parameters fixed. We took our best model and then changed the way we calculated the destruction rate to that of either TH85, BD96, or the complete H_2 molecule in Cloudy. Our results shown in Table 3 clearly demonstrate how approximations to the destruction rate can lead to dramatically different results. For the TH85 rate, the predicted column density is 4 orders of magnitude larger than that from either BD96 or the complete H_2 molecule. This difference suggests that treating the H_2 molecule as a two-level atom causes the calculation to overcompensate for the effects of self-shielding, which lowers the calculated destruction rate. The lower destruction rate then causes an overabundance of H_2 through the same nonlinear feedback that is seen in Figure 11. It appears that in general the BD96 dissociation rate approximates the Cloudy dissociation rate fairly well.

TABLE 3
VARIATION OF THE PREDICTED H_2 COLUMN DENSITY WITH TREATMENT OF THE DESTRUCTION RATE

Destruction Rate Treatment	$N(H_2)$ (cm^{-2})
TH85	1.5×10^{19}
BD96	5.0×10^{14}
Cloudy 96 (complete H_2 molecule)	3.3×10^{14}

A2. FORMATION RATES

In addition to testing the sensitivity of the predicted H_2 abundance to the destruction rate, we also tested the sensitivity of the H_2 abundance to the formation rate of H_2 by grain catalysis. TH85 use a formation rate given by

$$R_f = X\left(6 \times 10^{-17}\right)(T/300)^{0.5} S(T) \text{ cm}^3 \text{ s}^{-1}, \quad (7)$$

where T is the temperature (in kelvins) and $S(T)$ is the sticking coefficient taken from Hollenbach & McKee (1979). Again, we insert a scaling factor X to test how the H_2 abundance changes with formation rate.

Figure 11 also shows how scaling the formation rate affects the predicted H_2 abundance. Just as with the destruction rate, the final amount of H_2 is very sensitive to changes in the formation rate. Again, this is due to the nonlinear relationship between the rate and the H_2 density. Because the H_2 fraction depends on the grain formation rate and n in equation (5), scaling the formation rate will make the H_2 abundance increase/decrease, which in turn feeds back into equation (5) through n. This feedback quickly leads to large changes in H_2 formation for relatively small changes in X. Since the formation rate is dependent on the treatment of the grain physics and the observationally determined rate coefficient (Jura 1974), care must be taken to assure that both of these factors are determined to the highest possible precision.

A3. GRAIN-SIZE DISTRIBUTION

We ran one final test, to check how the H_2 column density changed when different grain distributions were considered. We ran a series of models with a density of 10^3 cm^{-3}, approximately corresponding to our best model density. We then varied G_0 from 1 to 10^6 in increments of 0.5 dex. This calculation was performed for both an Orion grain distribution (absence of small grains) and a standard ISM grain distribution, designed to reproduce the standard interstellar extinction curve ($R = 3.1$). This calculation, unlike the rest of our calculations, neglected hydrogen-ionizing radiation. We also stopped this calculation at a total hydrogen column density of 4×10^{21} cm^{-2}, as opposed to at just the atomic column density $N(H^0)$ used in all other calculations.

As shown in Figure 12, the final H_2 column density can be very sensitive to the grain-size distribution. For low values of G_0, both size distributions are effective in absorbing the H_2 dissociating continuum. This low dissociation rate allows all the available hydrogen to combine into H_2. As the value of G_0 is increased, a point is reached at which, for a given size distribution and total hydrogen column density, the H_2 dissociating continuum is not effectively absorbed. The value of G_0 at which this occurs will be smaller for grain-size distributions that are weighted toward large grains. Larger grains provide less extinction per unit mass, which in turn keeps the dissociation rate large over a greater depth into the cloud. Figure 12 shows that the critical value of G_0 at which the dissociation rate remains large (i.e., self-shielding no longer occurs) is about $10^{2.5}$ for Orion grains and about 10^4 for ISM grains. Over the range of $10^{2.5} < G_0 < 10^{4.5}$, differences in the predicted H_2 column density approaching 6 orders of magnitude can occur. This range of G_0 includes the value of about 10^4 that we estimate for the veil. Therefore, the anomalous grain-size distribution in the veil is capable of having a very important effect on the H_2 abundance. For $G_0 > 10^{4.5}$, the sensitivity of H_2 to grain size is lessened. For these high values of G_0, neither size distribution is effective in absorbing the H_2 dissociation continuum, which keeps the dissociation rate high. The H_2 column density will remain small and, as can be seen in equation (5), scale inversely with the dissociation rate. The grain-size distribution still affects the predicted H_2 abundance, because the larger grain sizes in Orion are less effective than the ISM grains in absorbing the UV continuum. The Orion grains also have less surface area per unit mass of hydrogen, which lowers the H_2 formation rate on grains relative to the ISM grain-size distribution. These combined effects cause the predicted H_2 column density to be $\sim$1.5 dex lower for our Orion grain-size distribution for $G_0 > 10^{4.5}$.

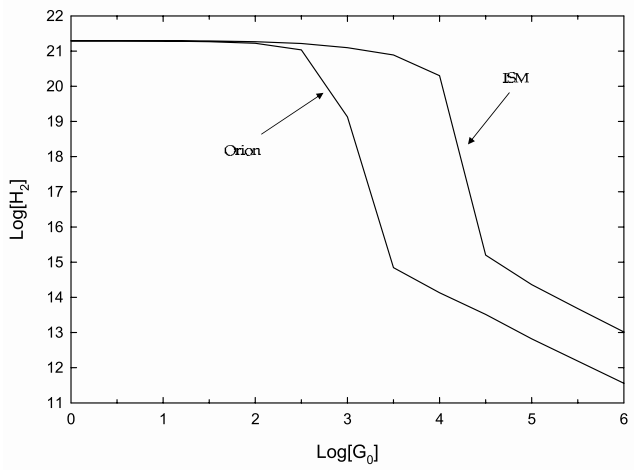

FIG. 12.—Column density of H_2 (cm^{-2}) for different grain-size distributions over a range of G_0. For $\log(G_0) < 2.5$, H_2 fully forms for both ISM and Orion grains. For larger values, the lack of small grains in the Orion distribution makes it less effective than ISM grains in shielding the H_2 dissociating continuum, and the dissociation rate becomes larger relative to the dissociation rate calculated using ISM grains. This process causes the two size distributions to differ by up to 6 orders of magnitude for some values of G_0.

The importance of using accurate formation and destruction rates is not new; Browning et al. (2003) also demonstrate this principal in a different context. However, it is not widely known that small deviations from the true formation and destruction rates can cause H_2 abundance predictions to vary by large amounts, at least for conditions similar to the veil. One must be sure that any assumptions or approximations to the formation and destruction rates do not significantly affect the final predictions. The best way to do this is to check the approximation versus the more refined, computationally expensive calculation. In the case of this paper, the TH85 destruction rates often led to results that differed significantly from observation. Our best model would not be allowed by observation if we had used the TH85 destruction rate. It was not until we calculated a destruction rate determined by using the complete H_2 molecule that we obtained results that were consistent with observational data.

REFERENCES

Abgrall, H., Roueff, E., & Drira, I. 2000, A&AS, 141, 297
Allison, A. C., & Dalgarno, A. 1969, At. Data, 1, 91
Armour, M., Ballantyne, D., Ferland, G., Karr, J., & Martin, P. G. 1999, PASP, 111, 1251
Baldwin, J. A., Ferland, G. J., Martin, P. G., Corbin, M. R., Cota, S. A., Peterson, B. M., & Slettebak, A. 1991, ApJ, 374, 580
Bally, J., O'Dell, C. R., & McCaughrean, M. J. 2000, AJ, 119, 2919
Bertoldi, F., & Draine, B. T. 1996, ApJ, 458, 222 (BD96)
Bohlin, R. C., & Savage, B. D. 1981, ApJ, 249, 109
Bottorff, M., Lamothe, J., Momjian, E., Verner, E., Vinkovic, D., & Ferland, G. 1998, PASP, 110, 1040
Browning, M. K., Tumlinson, J., & Shull, J. M. 2003, ApJ, 582, 810
Cardelli, J. A., Clayton, G. C., & Mathis, J. S. 1989, ApJ, 345, 245
Cazaux, S., & Tielens, A. G. G. M. 2002, ApJ, 575, L29
Chandrasekhar, S., & Fermi, E. 1953, ApJ, 118, 113
Crutcher, R. M., Troland, T. H., Goodman, A. A., Heiles, C., Kazes, I., & Myers, P. C. 1993, ApJ, 407, 175
Crutcher, R. M., Troland, T. H., Lazareff, B., Paubert, G., & Kazes, I. 1999, ApJ, 514, L121
Ferland, G. J. 2002, Hazy, A Brief Introduction to Cloudy, Dept. Phys. Astron. Internal Rep. 96.00 (Lexington: Univ. Kentucky)
Goudis, C. 1982, The Orion Complex: A Case Study of Interstellar Matter (Dordrecht: Reidel)
Heiles, C. 1997, ApJS, 111, 245
Heiles, C., & Troland, T. H. 2003, ApJ, 586, 1067
Hillenbrand, L. A., & Hartmann, L. W. 1998, ApJ, 492, 540
Hollenbach, D., & McKee, C. F. 1979, ApJS, 41, 555
Jura, M. 1974, ApJ, 191, 375
Launay, J. R., Le Dourneuf, M., & Zeippen, C. J. 1991, A&A, 252, 842
McKee, C. F. 1999, in The Origin of Stars and Planetary Systems, ed. C. J. Lada & N. D. Kylafis (Dordrecht: Kluwer), 29
Myers, P. C., & Goodman, A. A. 1988, ApJ, 326, L27
O'Dell, C. R. 2001, ARA&A, 39, 99
———. 2002, Rev. Mexicana Astron. Astrofis., 12, 12
O'Dell, C. R., Peimbert, M., & Peimbert, A. 2003, AJ, 125, 2590
O'Dell, C. R., Valk, J. H., Wen, Z., & Meyer, D. M. 1993, ApJ, 403, 678
O'Dell, C. R., & Yusef-Zadeh, F. 2000, AJ, 120, 382
Osterbrock, D. E. 1989, Astrophysics of Gaseous Nebulae and Active Galactic Nuclei (Mill Valley: University Science Books)
Osterbrock, D. E., Tran, H., & Veilleux, S. 1992, ApJ, 389, 305
Rubin, R., Simpson, J., Haas, M., & Erickson, E. 1991, ApJ, 374, 564
Savage, B. D., Bohlin, R. C., Drake, J. F., & Budich, W. 1977, ApJ, 216, 291
Savage, B., D., & Jenkins, E. B. 1972, ApJ, 172, 491
Shuping, R. Y., & Snow, T. P. 1997, ApJ, 480, 272 (SS97)
Spitzer, L. 1978, Physical Processes in the Interstellar Medium (New York: Wiley)
Takahashi, J., & Uehara, H. 2001, ApJ, 561, 843
Tielens, A. G. G. M., & Hollenbach, D. 1985, ApJ, 291, 722 (TH85)
Troland, T. H., Crutcher, R. M., Goodman, A. A., Heiles, C., Kazes, I., & Myers, P. C. 1996, ApJ, 471, 302
Troland, T. H., Heiles, C., & Goss, W. M. 1989, ApJ, 337, 342
van der Werf, P. P., & Goss, W. M. 1989, A&A, 224, 209
van der Werf, P. P., Goss, W. M., Heiles, C., Crutcher, R. M., & Troland, T. H. 1993, ApJ, 411, 247
van Hoof, P. A. M., Weingartner, J. C., Martin, P. G., Volk, K., & Ferland, G. J. 2001, in ASP Conf. Ser. 247, Spectroscopy Challenge of Photoionized Plasmas, ed. G. Ferland & D. W. Savin (San Francisco: ASP), 363
Walborn, N. R., & Panek, R. J. 1984, ApJ, 286, 718
Watson, W. D., Wiebe, D. S., & Crutcher, R. M. 2001, ApJ, 549, 377
Wolnievicz, L., Simbotin, I., & Dalgarno, A. 1998, ApJS, 115, 293
Zweibel, E. G., & McKee, C. F. 1995, ApJ, 439, 779